Chapter 4

Millimeter-Wave Multi-Port Front-End Receivers: Design Considerations and Implementation

Chaouki Hannachi and Serioja Ovidiu Tatu

Additional information is available at the end of the chapter

http://dx.doi.org/10.5772/intechopen.72715

Abstract

This chapter covers recent achievements on the integrated 60 GHz millimeter-wave front-end receiver based on the multi-port (six-port) concept. For this purpose, the design procedure of a fully integrated 60 GHz multi-port (six-port) front-end receiver implemented on a thin ceramic substrate (ε_r = 9.9, h = 127 μm) using an miniature hybrid microwave integrated circuit (MHMIC) fabrication process is presented in detail. All components constituting the proposed front-end receiver including an 8 × 2 antenna array, a low-noise amplifier (LNA), a six-port circuit, and the RF power detectors are presented and characterized separately before they are integrated into the final front-end receiver prototype. The performance of the latter has been experimentally evaluated in terms of various M-PSK/M-QAM demodulations. The obtained demodulation results are very satisfactory (the constellation points for all considered M-PSK/M-QAM schemes are very close to the ideal locations), demonstrating and confirming the high ability of the proposed 60 GHz millimeter-wave six-port front-end receiver to operate as a high-performance quadrature demodulator, without any calibration, for modulation schemes up to 32 symbols.

Keywords: demodulation, front-end, low power, MHMIC, millimeter-wave, receiver, six-port, 60 GHz

1. Introduction

In 2001, the Federal Communications Commission (FCC) allocated several GHz in the frequency band around 60 GHz for unlicensed use. In fact, this unlicensed millimeter-wave frequency band is available in North America and Korea (57–64 GHz), as well as in Europe and Japan (59–66 GHz) [1, 2]. The main characteristic of this frequency band is the very high level of attenuation due to the extremely high atmospheric absorption (17 dB/Km), in addition

to higher loss in common building materials, which make 60 GHz communication most suitable for short-range wireless applications, several meters for low power to max 1 km for backhaul solutions. However, to operate reliably at even short ranges, 60 GHz communication systems must also employ a highly focused, narrow-beam antenna to increase the level of signal available to the target receiver.

Today, the demand for high-data-rate wireless communications and broadband transceiver/receiver systems with reduced hardware requirements and high flexibility is highly increased. However, the existing hardware architectures for radio communication systems suffer from a number of limitations including high cost, design complexity, as well as high power consumption. For instance, for most mixers in conventional receivers, to obtain a good conversion gain, the power of the local oscillator must be more than 10 dBm, which is a relatively high power level compared to other alternatives reported in literature [3]. Moreover, in conventional receiver systems, the phase noise of the local oscillator (LO) is transformed directly into the phase noise in the baseband. This results in neighbor channel interference, usually caused by reciprocal mixing, consequently decreasing the selectivity of the receiver [1].

Radio architectures having a potential to get beyond the previously mentioned limitations include radio communication systems based on multi-port architectures. The design simplicity combined with the wideband characteristics of multi-port receiver structures may provide RF receiver architectures, which can solve many of the current challenges of receiver systems. It provides a straightforward approach for broadband operations, low power consumption, and low manufacturing costs, making it a serious candidate for various indoor millimeter-wave wireless applications [4, 5].

In the recent years, several designs of multi-port (six-port) circuits have been investigated and presented in literature. They range from microstrips to LC lumped element designs, for different microwave and millimeter-wave frequency bands [6]. The first reported multi-port circuit was employed in the 1970s by Glenn F. Engen and Cletus A. Hoer as an alternative solution to network analyzers for the measurement of complex scattering parameters [7, 8]. A couple of years later, it was used in radar applications and has recently been proposed as an alternative to the conventional receiver architectures such as the homodyne and heterodyne receivers.

In this chapter, a fully integrated 60 GHz front-end receiver based on the multi-port (six-port) technique is presented and analyzed. All parts composing the proposed front-end receiver such as an 8×2 antenna array, a low-noise amplifier (LNA), a six-port circuit, and the power detectors are presented and characterized separately. This chapter is therefore organized as follows. First, Section 2 gives a comprehensive overview on the MHMIC fabrication process used to manufacture the proposed 60 GHz front-end receiver prototype. Next, Section 3 shows the theoretical concept of the six-port circuit and how it operates as an amplitude/phase discriminator; moreover, it describes in detail the basic building blocks of the designed 60 GHz front-end receiver. The experimental characterization procedure and the obtained measurement results, as well as the final fabricated front-end receiver prototype with the experimental M-PSK/M-QAM demodulation results are also discussed in the same section. Finally, a conclusion is drawn.

http://dx.doi.org/10.5772/intechopen.72715

2. MHMIC fabrication process

Today, there are few promising high-quality fabrication processes, offering potentially low-cost and highly integrated millimeter-wave components, such as the monolithic microwave integrated circuit (MMIC) based on GaAs, silicon, or SiGe technology for large-scale production and the miniature hybrid microwave integrated circuit (MHMIC) for prototyping or small-scale production [9]. The latter adopts a thin-film process in which a wide range of passive components are fabricated on an alumina substrate having typically a high dielectric constant. These components are not limited only to the basic lumped passive components such as thin-film resistors, spiral inductors, and overlay capacitors, but they also include a large number of RF passive circuits including power dividers, directional couplers, printed antennas, and filters. The active devices such as diodes, power amplifiers (PAs), and low-noise amplifiers (LNAs) are implemented at the end of the process, using gold wire bonding technology.

The most frequently used materials for the substrate metallization are gold, copper, or copper-gold. High-precision thin-film resistors are typically implemented using nichrome or tantalum nitride films on a thin-film ceramic substrate. However, various processing techniques are usually used, such as photolithography techniques, e-beam, and, more recently, the excimer laser micromachining [10].

It is to be noted that the choice of a thin substrate is due to the reduced guided wavelength in high-permittivity ceramic substrates. In order to keep the required circuit aspect ratio (the guided wavelength versus the line width), the substrate thickness has to be as thin as possible. The optimal choice for frequencies higher than 60 GHz is the 127-μm-thick alumina substrate that is commercially available. This substrate is also easily compatible with the regular 100-μm-thick MMIC active components, to be integrated with planar passive MHMICs. MMIC chips are implemented in rectangular cuts on ceramics, on the top of the same metallic fixture, allowing thermal dissipation and easy wire bonding with MHMIC components, which are typically at the same height.

The MHMIC technology represents today an excellent alternative for low-cost and rapid prototyping of highly miniaturized circuits with improved performances at millimeter-wave frequencies up to 86 GHz [6].

3. Multi-port (six-port) circuit-based front-end receivers

The six-port (multi-port) quadrature down-conversion is an innovative approach in millimeter-wave technology. A comprehensive theory, validated by various simulations and measurements of 60 GHz (V-band) direct conversion receivers, has been presented in literature over the recent years [11, 12].

The block diagram in **Figure 1** highlights the operation principle of a front-end receiver based on a six-port circuit to demodulate RF signals. This structure is composed of three 90° hybrid

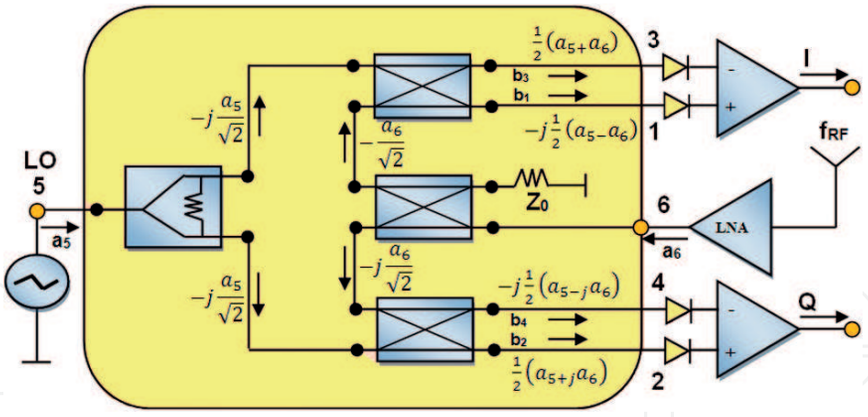

Figure 1. Block diagram of a six-port circuit-based front-end receiver.

couplers and a Wilkinson power divider. The proposed architecture makes possible to obtain, from output power measurements, the phase difference and the amplitude ratio between an unknown signal from the antenna (a_6) and the reference signal coming from a local oscillator (a_5).

The output signals b_i can be expressed as a function of the signals a_i and the S-parameter S_{ij} by the following linear relationship:

$$b_i = \sum_{j=1}^{6} S_{ij} a_j, \qquad i = 1, \ldots, 6 \tag{1}$$

The S_{ij} parameters of the six-port circuit can be obtained directly from **Figure 1**. For that purpose, the S-parameter matrices [S] of the 90° hybrid coupler and the Wilkinson power divider are employed. The corresponding matrices are given in Eqs. (2) and (3):

$$[S] = \frac{1}{\sqrt{2}} \begin{bmatrix} 0 & j & 1 & 0 \\ j & 0 & 0 & 1 \\ 1 & 0 & 0 & j \\ 0 & 1 & j & 0 \end{bmatrix} \tag{2}$$

$$[S] = -j\frac{1}{\sqrt{2}} \begin{bmatrix} 0 & 1 & 1 \\ 1 & 0 & 0 \\ 1 & 0 & 0 \end{bmatrix} \tag{3}$$

Thus, the global S-parameter matrix [S] of the six-port circuit in **Figure 1** is obtained by Eq. (4):

$$[S] = \frac{1}{2} \begin{bmatrix} 0 & 0 & 0 & 0 & -j & j \\ 0 & 0 & 0 & 0 & 1 & j \\ 0 & 0 & 0 & 0 & 1 & 1 \\ 0 & 0 & 0 & 0 & -j & -1 \\ -j & 1 & 1 & -j & 0 & 0 \\ j & j & 1 & -1 & 0 & 0 \end{bmatrix} \tag{4}$$

Using Eq. (4), we may obtain the formulas of the four waveforms, b_1, b_2, b_3, and b_4, as a function of the two incident waves a_5 and a_6, as described in Eq. (5):

$$\begin{cases} b_1 = -j\dfrac{a_5}{2} + j\dfrac{a_6}{2} \\ b_2 = \dfrac{a_5}{2} + j\dfrac{a_6}{2} \\ b_3 = \dfrac{a_5}{2} + \dfrac{a_6}{2} \\ b_4 = -j\dfrac{a_5}{2} - \dfrac{a_6}{2} \end{cases} \tag{5}$$

In order to simplify calculations, we assume that the RF signals resulting from the antenna a_6 and the local oscillator (LO) a_5 have an amplitude ratio α, a phase difference $\Delta\varphi(t) = \varphi_6(t) - \varphi_5$, and a frequency difference $\Delta\omega = \omega - \omega_0$ ($\omega = 2\pi f$). Therefore, these signals can be expressed by the following equations [11]:

$$a_5 = a \cdot e^{j\left(\omega_0 \cdot t + \varphi_5\right)} \tag{6}$$

$$a_6 = \alpha \cdot a \cdot e^{j\left(\omega_0 \cdot t + \varphi_6(t)\right)} = \alpha \cdot a_5 \cdot e^{j(\Delta\omega \cdot t + \Delta\varphi(t))}. \tag{7}$$

By replacing the expressions of signals a_5 and a_6 in the system of Eq. (5), we obtain

$$b_1(t) = -j\frac{a}{2} \cdot e^{j\left(\omega_0 t + \varphi_5\right)} \cdot \left[1 + \alpha \cdot e^{j(\Delta\omega \cdot t + \Delta\varphi(t) + \pi)}\right] \tag{8}$$

$$b_2(t) = \frac{a}{2} \cdot e^{j\left(\omega_0 t + \varphi_5\right)} \cdot \left[1 + \alpha \cdot e^{j\left(\Delta\omega \cdot t + \Delta\varphi(t) + \frac{\pi}{2}\right)}\right] \tag{9}$$

$$b_3(t) = \frac{a}{2} \cdot e^{j\left(\omega_0 t + \varphi_5\right)} \cdot \left[1 + \alpha \cdot e^{j(\Delta\omega \cdot t + \Delta\varphi(t))}\right] \tag{10}$$

$$b_4(t) = -j\frac{a}{2} \cdot e^{j\left(\omega_0 t + \varphi_5\right)} \cdot \left[1 + \alpha \cdot e^{j\left(\Delta\omega \cdot t + \Delta\varphi(t) - \frac{\pi}{2}\right)}\right] \tag{11}$$

It should be noted that the signals at the intermediate frequency (IF) band are the results of connecting the four six-port circuit outputs to the power detectors (see **Figure 1**). We consider that the power delivered at the output of each ideal power detector is proportional to the square of the RF signal magnitude [11, 13]. Under these conditions

$$v_i = K_i \cdot |b_i|^2 = K_i \cdot b_i \cdot b_i^*, \qquad i = 1, \ldots, 4 \tag{12}$$

Given that the power detectors are identical ($K_i = K$), then

$$v_1(t) = K\frac{a^2}{4} \cdot \left\{1 + \alpha^2 - 2 \cdot \alpha \cdot \cos\left[\Delta\omega \cdot t + \Delta\varphi(t)\right]\right\} \tag{13}$$

$$v_2(t) = K\frac{a^2}{4}\cdot\left\{1 + \alpha^2 - 2\cdot\alpha\cdot\sin\left[\Delta\omega\cdot t + \Delta\varphi(t)\right]\right\} \tag{14}$$

$$v_3(t) = K\frac{a^2}{4}\cdot\left\{1 + \alpha^2 + 2\cdot\alpha\cdot\cos\left[\Delta\omega\cdot t + \Delta\varphi(t)\right]\right\} \tag{15}$$

$$v_4(t) = K\frac{a^2}{4}\cdot\left\{1 + \alpha^2 + 2\cdot\alpha\cdot\sin\left[\Delta\omega\cdot t + \Delta\varphi(t)\right]\right\} \tag{16}$$

In order to generate quadrature signals IF/IQ, we use differential amplifiers in the intermediate frequency band, at outputs 1, 3, and 2, 4 (see **Figure 1**):

$$v_{IF}^{I}(t) = A_{IF}\cdot[v_3(t) - v_1(t)] = \alpha\cdot K\cdot a^2\cdot A_{IF}\cdot\cos\left[\Delta\omega\cdot t + \Delta\varphi(t)\right] \tag{17}$$

$$v_{IF}^{Q}(t) = A_{IF}\cdot[v_4(t) - v_2(t)] = \alpha\cdot K\cdot a^2\cdot A_{IF}\cdot\sin\left[\Delta\omega\cdot t + \Delta\varphi(t)\right] \tag{18}$$

A second frequency conversion followed by low-frequency filtering is performed. The I/Q baseband signal formulas are thus obtained:

$$I(t) = \frac{1}{2}\cdot\alpha\cdot K\cdot a^2\cdot A_{IF}\cdot A_{BB}\cdot\cos\left[\Delta\varphi(t)\right] \tag{19}$$

$$Q(t) = \frac{1}{2}\cdot\alpha\cdot K\cdot a^2\cdot A_{IF}\cdot A_{BB}\cdot\sin\left[\Delta\varphi(t)\right] \tag{20}$$

In fact, the baseband I/Q signal can be expressed in the complex plane by the following equation:

$$\Gamma(t) = I(t) + Q(t) = \frac{1}{2}\cdot\alpha\cdot K\cdot a^2\cdot A_{IF}\cdot A_{BB}\cdot e^{j\Delta\varphi(t)} \tag{21}$$

This expression shows that the terms A_{IF} and A_{BB} are related to the intermediate frequency (IF) band and baseband (BB) amplification. The receiver works in both architectures: heterodyne, according to Eqs. (17) and (18), and homodyne, according to Eqs. (19) and (20). The amplitude ratio α and the phase difference, $\Delta\varphi(t) = \varphi_6(t) - \varphi_5$, can be obtained in baseband. This relationship between the RF domains and the intermediate (IF) band as well as the baseband has highlighted the role of the six-port circuit (reflectometer) as a phase, frequency, and amplitude discriminator [11].

3.1. Multi-port (six-port) circuit design and characterization

A broadband six-port circuit with an improved symmetry and rounded shapes has been designed on a thin alumina substrate (ε_r = 9.9 and h = 127 μm) using the novel Wilkinson power divider/combiner and the three rounded 90° hybrid couplers [9]. The central design frequency is 60.5 GHz, in the center of an unlicensed frequency band (57 to 64 GHz).

It should be noted that all measurements are performed from 60 GHz, due to the available measurement setup capabilities (WR-12 rectangular waveguide modules for the 60–90 GHz

millimeter-wave extension of the VNA). However, extrapolation of measurements and comparison with simulations allow assessing the circuit behavior from 57 to 60 GHz. The microphotograph in **Figure 2(a)** shows the fabricated six-port circuit ready for port 4 to port 5 measurements using a coplanar line to microstrip transition and a precise on-wafer measurement structure equipped with ground-signal-ground (GSG)-150 μm coplanar probes, as shown in **Figure 2(b)**.

As can be seen in **Figure 2(a)**, all remaining ports are terminated by matched loads (50 Ω), integrated on the same substrate using a 100 Ω per square titanium oxide thin layer. In order to avoid the metalized via holes that are complicated to achieve with accuracy and repeatability at millimeter-wave frequencies, the 50 Ω loads use a quarter wavelength open stubs as millimeter-wave RF short circuits (see ports 1, 2, 3, and 4). The outer six-port dimensions are more or less 6.5 mm by 6.5 mm.

In order to ensure the accuracy of S-parameter measurements, the on-wafer through-reflect-line (TRL) calibration technique is employed, using the calibration kits on the same ceramic alumina substrate as the devices under test (DUT) [9]. Its standards are shown in **Figure 3**. It consists of a thru line (T), two open circuits as reflect (R), and a short line (L). Due to the fragility of the very thin gold layer metallization (1 μm), multiple identical standards are designed on the same ceramic substrate to ensure repeatability and success of on-wafer calibrations and S-parameter measurements.

Figure 4 shows the typical return loss measurement at port 6 (RF input) and port 5 (LO input), as well as the isolation between them. As can be seen, at the center operating frequency, around 60 GHz, all values are better than 20 dB. Moreover, the measured values are better than 15 dB at the highest frequency (64 GHz) of the unlicensed frequency band. In fact, the achieved high isolation level is a result of employing a highly isolated round-shaped Wilkinson power divider with a high-precision integrated resistor, which has been implemented with accuracy on the 100 Ω per square titanium oxide thin layer, using MHMIC technology [14], as described earlier.

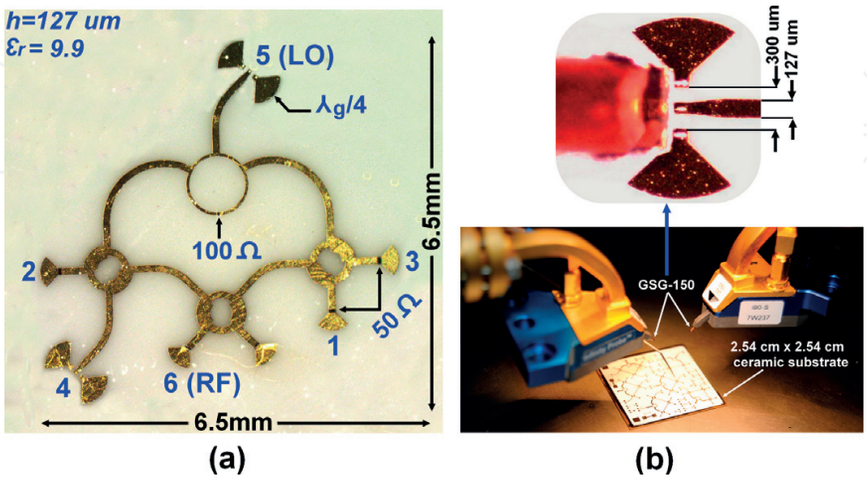

Figure 2. Microphotograph of the fabricated millimeter-wave six-port circuit: (**a**) the on-wafer S-parameter measurement configuration and (**b**) the on-wafer S-parameter measurement process using GSG-150 μm coplanar probes.

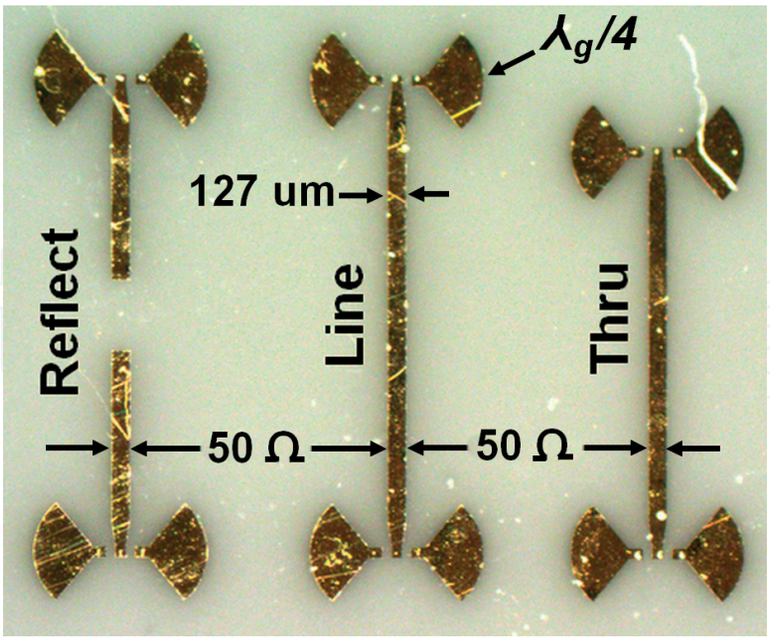

Figure 3. Microphotograph of TRL calibration kit.

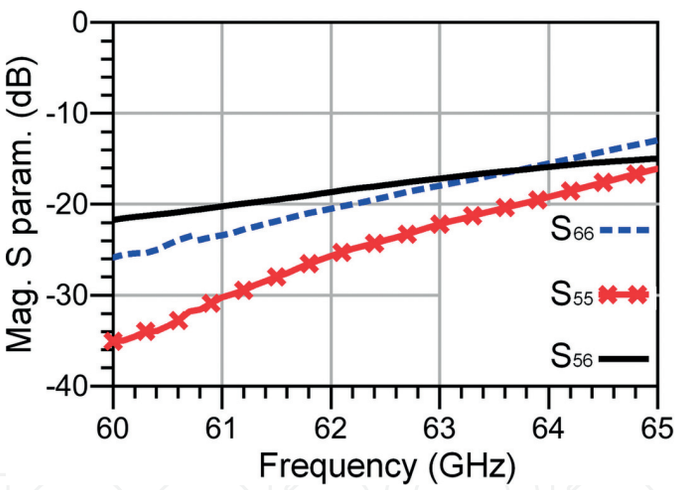

Figure 4. Measured RF inputs return loss and isolation for the fabricated six-port circuit.

The measured return losses at output ports (1, 2, 3, and 4) are illustrated in **Figure 5**. These results exhibit a good matching at all ports, with better than 25 dB around the operating frequency of 60 GHz while keeping a good matching level for the rest of the band (better than 15 dB at the highest frequency (64 GHz)).

Figure 6 shows the measured transmission coefficient results, commonly known as the power splitting between the LO port 5 and two adjacent outputs (ports 2 and 4), as well as between the RF port 6 and two other adjacent outputs (ports 1 and 3). As can be seen, the measured transmission coefficients are close to the value of −6 dB over the considered frequency band, according to the six-port theory. However, around the center frequency of 60 GHz, the

http://dx.doi.org/10.5772/intechopen.72715

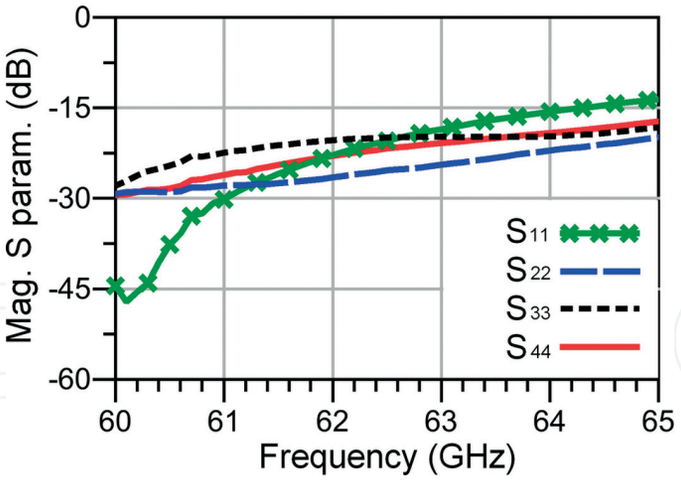

Figure 5. Measured RF outputs return loss (ports 1, 2, 3, and 4) for the fabricated six-port circuit.

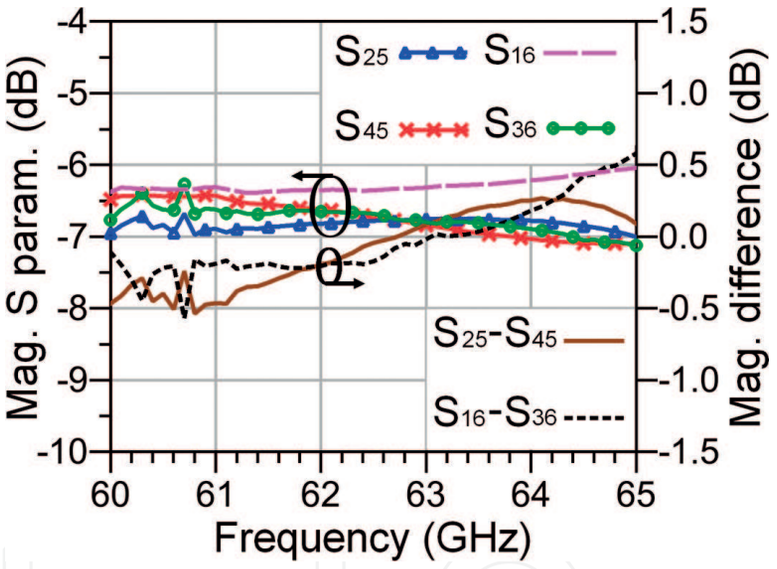

Figure 6. Typical transmission magnitude measurements for the fabricated six-port circuits.

maximum supplementary insertion loss does not exceed 0.6 dB, reaching approximately 1.2 dB at the upper edge. The magnitude unbalance between two pairs of outputs is close to 0 dB at 62.5 GHz and is less than 0.5 dB over the frequency band of interest. It should be noted that due to the high symmetry of the designed circuit, similar results are obtained between port 5 and the other two six-port outputs (1, 3). The same is valid for the transmission coefficient results between RF port 6 and outputs (2, 4).

Figure 7 shows the phase difference between the two typical transmission S-parameters, S_{52} and S_{54}, as well as S_{61} and S_{63}. The obtained results show two quasi-parallel characteristics. The measured phase difference between each two adjacent ports is close to the quadratic reference of 90°. However, the observed phase difference error is less than ±2° up to 64 GHz.

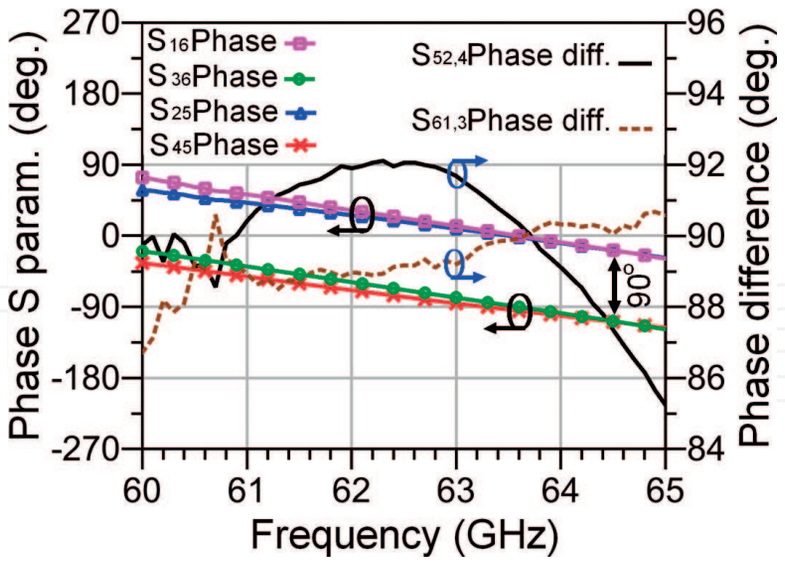

Figure 7. Typical transmission phase measurements for the fabricated six-port circuits.

The plot of the q_i points using the S-parameter measurement results of the proposed six-port circuits is shown in **Figure 8**. As can be seen, the q_i points are positioned equidistantly from the origin and angularly spaced by 360° divided their number (i = 4 in this case). These results underline the performance of the fabricated six-port circuit and prove the high accuracy location of the q_i points over the considered 60 GHz frequency band. Consequently, the magnitudes of the q_i points are equal and closer to 1, while the argument difference is closer to 90° between two corresponding q_i points.

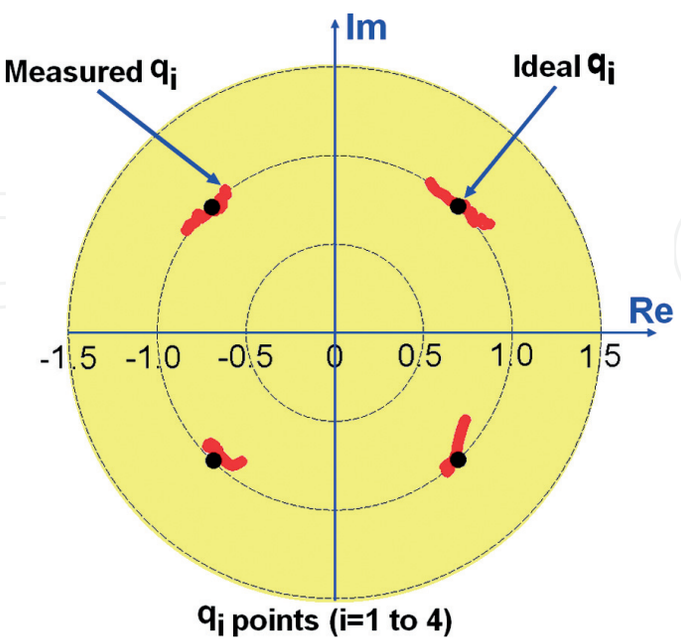

Figure 8. The q_i points of the fabricated six-port circuit for the considered frequency band 60–65 GHz.

3.2. Millimeter-wave power detector design and characterization

As we have seen in the previous section, to recover the low IF or the baseband signals, the implementation of power detectors at the four outputs of the six-port circuit is required. For that purpose, the HSCH-9161 millimeter-wave zero-bias GaAs Schottky diode of Keysight Technologies is selected for power detection, due to its broadband and high-speed properties [15, 16]. The typical configuration of the power detector usually includes the Schottky diode followed by a low-pass filter to extract the DC component, as illustrated in **Figure 9**.

The nonlinear characteristic between the current $i(t)$ that passes through the diode and the input RF voltage $V_{RF}(t)$ is generally described by the Schottky law. By neglecting the parasitic resistance of the diode, this characteristic will be expressed by

$$i(t) = I_s\left[\exp\left(\frac{q_o v_{RF}(t)}{nKT}\right) - 1\right] \tag{22}$$

where I_s is the saturation current, q_o is the charge of the electron, n is the coefficient of ideality, K is the Boltzmann constant, and T is the temperature.

Knowing that the voltage $V_{RF}(t)$ can be expressed by

$$v_{RF}(t) = A\cdot\cos(\omega_{RF}t), \quad \omega_{RF} = 2\pi f_{RF} \tag{23}$$

On the other hand, considering that the input signal $V_{RF}(t)$ has a low power and that it satisfies the condition, $A < V_T$, then we can reexpress Eq. (22) by using the limited development of the exponential function to obtain

$$i(t) = I_s\left[\left(\frac{v_{RF}(t)}{nV_T}\right) + \frac{1}{2}\left(\frac{v_{RF}(t)}{nV_T}\right)^2 + \ldots\right] \tag{24}$$

Moreover, the low-frequency equivalent circuit at the output of the power detector may be presented as follows (**Figure 10**) [16]:

The dynamic resistance of the diode R_V represents the video resistance [16]. The latter with the resistor R and the capacitor C forms a first-order low-pass filter having a cutoff frequency f_c:

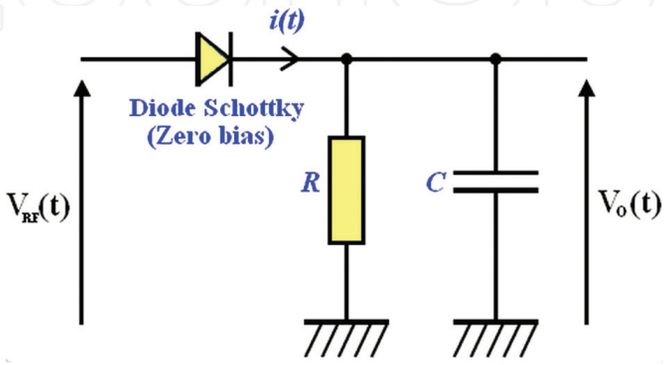

Figure 9. Typical configuration of a zero-bias Schottky diode-based power detector.

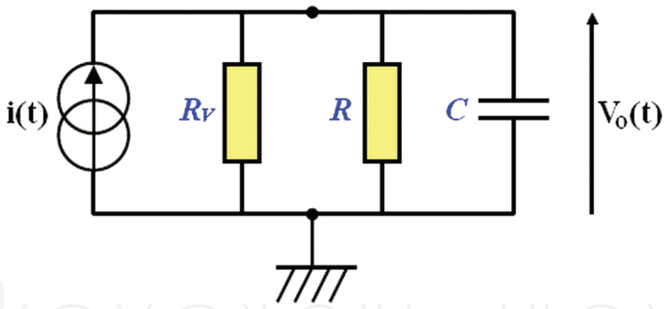

Figure 10. Equivalent circuit for the output of the Schottky diode-based power detector.

$$f_c = \frac{R_v + R}{2\pi R_v RC} \tag{25}$$

By choosing a low-frequency cutoff f_c compared to the RF input frequency of the power detector, the output voltage V_o(t) will therefore be proportional to the low-frequency or baseband (BB) components of the current *i(t)*, particularly to the quadratic term of Eq. (24).

Then, by replacing the expression of the input RF voltage given by Eq. (23) in Eq. (24) and taking into account only the quadratic term of the equation, we obtain

$$i(t) = \frac{I_S}{2}\left(\frac{A\cdot\cos\left(2\pi f_{RF}t\right)}{V_T}\right)^2 \tag{26}$$

After a low-pass filtering operation, the output voltage will be expressed as follows:

$$v_o(t) = \frac{R\cdot R_V}{R + R_V}\left(\frac{I_S}{4{V_T}^2}\right)^2\cdot A^2 = \alpha\cdot P_{RF} \tag{27}$$

The coefficient α represents the sensitivity of the power detector, usually expressed in volts/watt. According to the formula, it can be seen that for the low power levels, the detector can perform power detection because the output voltage of the detector is proportional to the square of the input signal amplitude or, in other words, to the power of the RF signal.

The photograph of the fabricated millimeter-wave power detector circuit used in the proposed front-end receiver architecture is shown in **Figure 11**. It comprises three main parts: the input impedance matching circuit, an HSCH-9161 millimeter-wave GaAs Schottky diode (zero bias), and the detected DC voltage output circuit. Obviously, all parts are designed and implemented on a thin ceramic substrate (ε_r = 9.9, h = 127 μm), using an MHMIC fabrication process. The input of the diode is well matched to 50 Ω using an accurate impedance matching stage to achieve the maximum transmission of the RF signal to diode input. The proposed impedance matching networks include an open-circuit stub of 0.16λ in parallel with the main 50 Ω microstrip line for matching purposes, as well as quarter-wave length-paralleled radial stubs attached to a metalized via-hole through a high-impedance quarter-wave length microstrip line, to prevent the RF signal leakage, providing DC ground. The integrated high-precision resistors of 100 Ω (parallel) are implemented on a 100 Ω per square titanium oxide thin layer

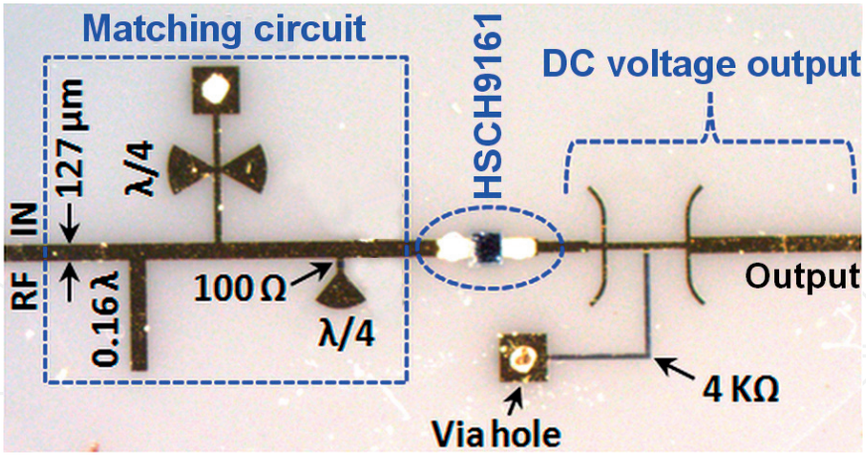

Figure 11. Photograph of the fabricated power detector prototype.

and have the role of providing resistive input impedance that enables broadband operation [15]. The quarter-wave length radial stub provides RF ground.

At the diode output, a broadband low-pass filtering made from two pairs of quarter-wave reflectors has been performed. This operation allows extraction of the DC voltage signals while suppressing all undesired higher-frequency components. In order to maximize the output detection voltage, a high-impedance integrated grounded resistor of 4 KΩ has also been added at the diode detector output. It uses the same 100 Ω per square titanium oxide thin layer.

The simulated and measured return loss at the RF input of the fabricated power detector circuit is compared, with good agreement, in **Figure 12**. As can be observed, the measured impedance bandwidth at −10 dB covers the frequency range of 3.8 GHz, from 60 to 63.8 GHz, which represents a bandwidth of 6.13%, at the center frequency of 61.9 GHz.

The simulated and the measured results of output power versus input power, at 61.9 GHz, are shown in **Figure 13**. As can be seen, a good concordance is achieved between measurement and simulation based on the diode model using the Keysight's Advanced Design System

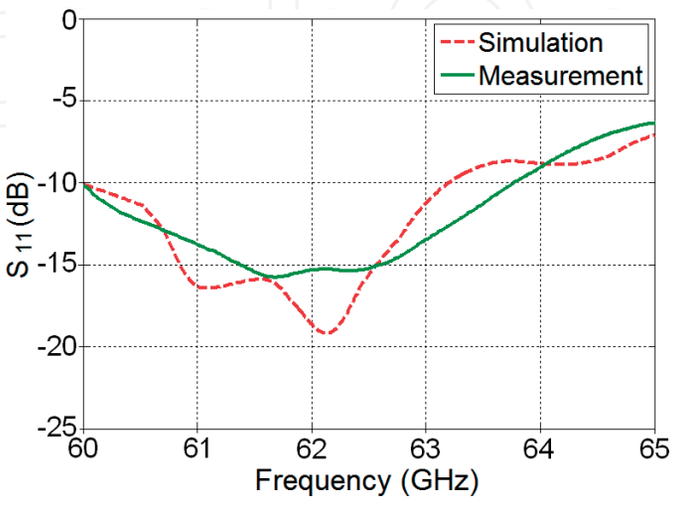

Figure 12. Simulated and measured return loss of the fabricated millimeter-wave power detector.

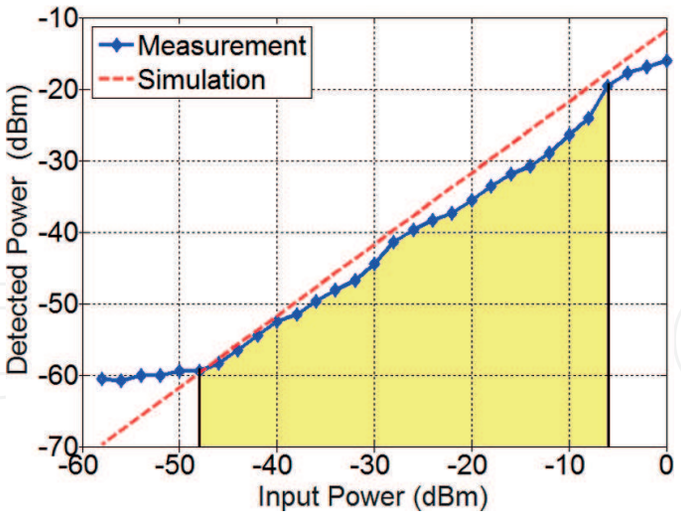

Figure 13. Simulated and measured detected power versus input power at 61 GHz.

(ADS) software. The proposed power detector shows a measured dynamic range (detection range) in the linear region of more than 42 dB. A high sensitivity is also achieved; the minimum detectable input power level using digital voltmeter is approximately −48 dBm.

3.3. V-band low-noise amplifier (LNA) implementation

A low-noise amplifier (LNA) represents the head amplifier of the receiving chain. It is often mounted as close as practical to the antenna, in order to amplify signals having a very low power level. However, the amplification of the signal received by the amplifier must meet two important criteria: maintain a stable and appropriate gain and control the noise figure (NF) of the receiver. In other words, a trade-off between the noise factor and the gain is therefore necessary in the LNA design. Generally, the noise factor F describes the signal-to-noise ratio degradation caused by the RF chain components. It is defined as the ratio of the input SNR (signal-to-noise ratio) to the output SNR of the receiver system:

$$SNR = \frac{SNR_{IN}}{SNR_{OUT}} \tag{28}$$

In the designed front-end receiver prototype, the low-noise amplifier TGA4600 from TriQuint Semiconductor company has been selected. The latter has a reasonable noise factor, $NF = 4$ dB, allowing to significantly limit the noise contribution of the reception chain. The typical implementation of the employed low-noise amplifier with gold bonding wires and ribbons on a ceramic substrate is illustrated in a photograph of **Figure 14**. Typical characteristics at 60 GHz are also presented in **Table 1**.

3.4. Millimeter-wave microstrip antenna array design

Millimeter-wave microstrip patch antennas are a promising alternative to the future wireless communication technologies in various fields including military, industrial, and commercial [17]. This is primarily due to their small size, low cost, and light weight, as well as the ease of

http://dx.doi.org/10.5772/intechopen.72715

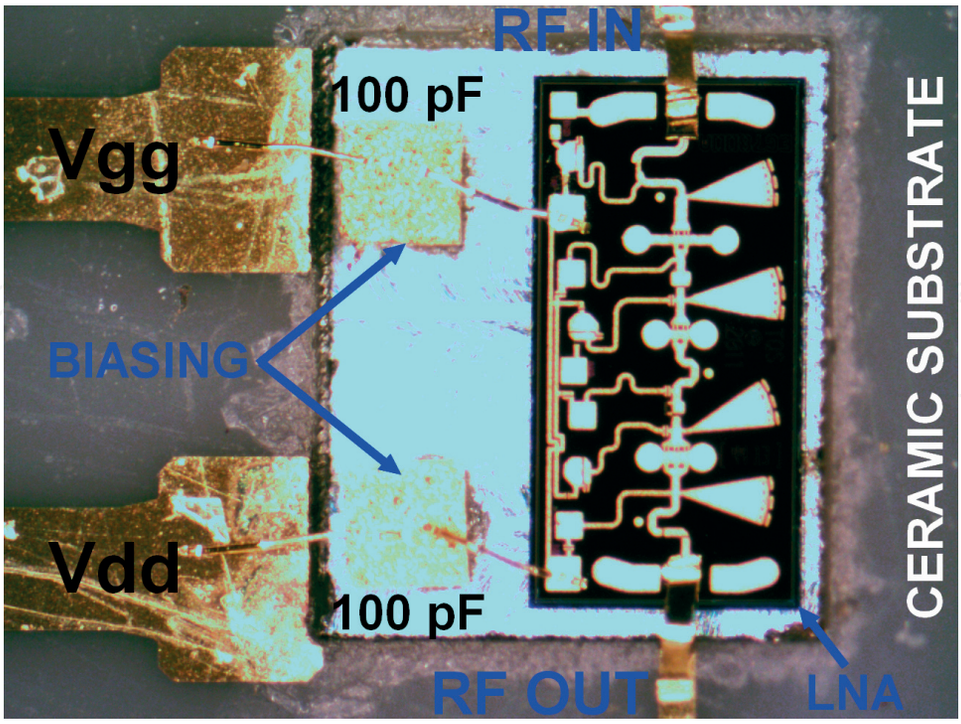

Figure 14. Photograph of typical low-noise amplifier TGA4600 implementation on a thin ceramic substrate.

Technology	0.15 μm 3MI pHEMT
NF	4 dB
Gain	13 dB
Typical frequency range	57–65 GHz
Input/output impedance	50 Ω
Input/output return loss	26 dB/6 dB
Reverse isolation	20 dB
Stability factor	>1

Table 1. Typical characteristics of TGA4600 low-noise amplifier at 60 GHz.

fabrication and integration with any planar fabrication technology, such as the miniature hybrid microwave integrated circuit (MHMIC) or the monolithic microwave integrated circuit (MMIC) [18].

In this section, a high-gain 8 × 2 element microstrip patch antenna array has been designed to be integrated in the proposed 60 GHz millimeter-wave RF front-end receiver prototype, for high-data-rate indoor wireless applications. The proposed array configuration was simulated using the Advanced Design System (ADS) software from Keysight Technologies and tested using the vector network analyzer (E8362B) with millimeter-wave extension modules of the same company.

The geometry of the fabricated microstrip 8 × 2 antenna array, including its single patch element, is shown in the photograph at **Figure 15**. The proposed array architecture adopts a corporate feed network connected to a 50 Ω coplanar feed line to carry out on-wafer measurements through ground-signal-ground (GSG)-150 μm coplanar probes. The employed corporate microstrip feed network includes a Wilkinson power divider/combiner and multiple tee junctions, which are interconnected by microstrip lines of 50 Ω and 70.7 Ω characteristic impedances to allow impedance matching, as well as better control over the phase and amplitude of each single patch element. This approach provides high directivity, improves radiation efficiency, and reduces beam fluctuations, over the suggested frequency range, compared to other array configurations [17]. The geometrical parameters of the proposed antennas are Wa = 18.56 mm, La = 5.01 mm, W = 1.07 mm, L = 0.74 mm, d = 1.43 mm, and d_1 = 1.60 mm.

The simulated and measured return losses of the single patch antenna, as well as the 8 × 2 microstrip array, are compared in **Figure 16**. As can be seen, good concordances are achieved

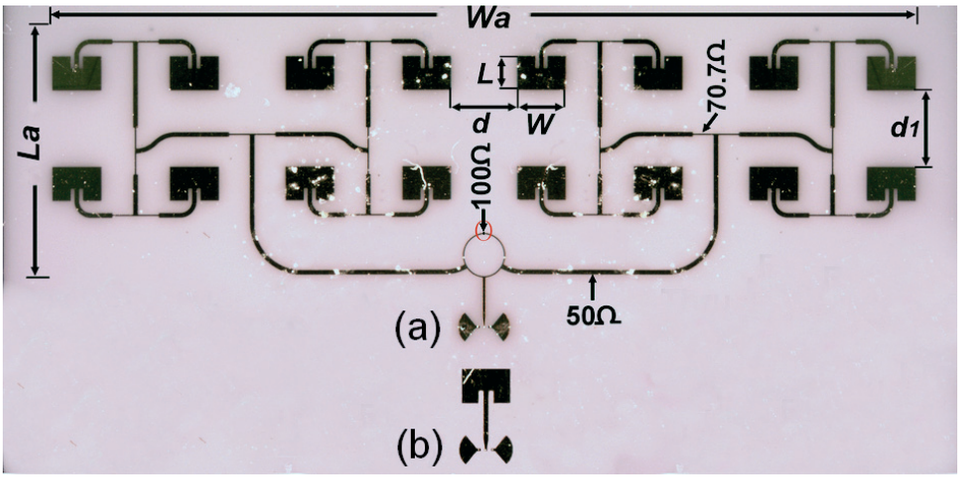

Figure 15. Photograph of the fabricated prototype with the geometrical parameters of (**a**) the 8 × 2 microstrip array antenna and (**b**) the single patch.

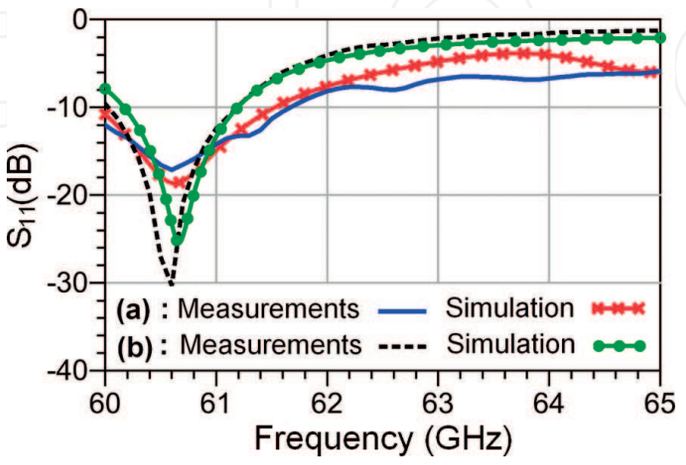

Figure 16. Measured and simulated return loss of (**a**) the 8 × 2 microstrip array antenna and (**b**) the single patch.

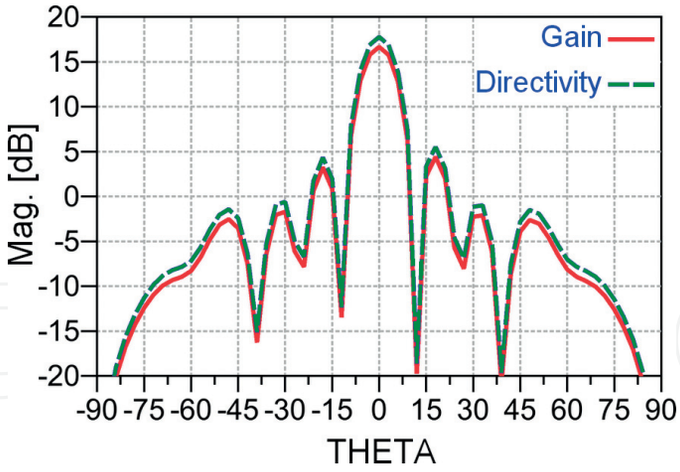

Figure 17. 2D simulated radiation pattern of the proposed 8 × 2 microstrip antenna array at 60.5 GHz.

over the considered frequency range (60–65 GHz). However, the −10 dB antenna bandwidths cover from 60 GHz to 61.2 GHz for the single patch and from 60 GHz to 61.7 GHz for the 8 × 2 microstrip array, which represent, respectively, bandwidths of 1.2 GHz (2%) and 1.7 GHz (2.83%), respectively.

The simulated 2D radiation pattern in E-plane at 60.5 GHz is illustrated at **Figure 17**. As can be observed, the simulated radiation pattern maintains a high symmetry and a good broadside radiation pattern. The maximum gain and directivity are 16.8 dB and 17.9 dB, respectively. The simulated antenna efficiency is around 77.43%. The half-power beamwidth (HPBW) is about 12°, and the first-side lobe is about 12.8 dB below the main lobe.

3.5. Millimeter-wave multi-port (six-port) front-end receiver implementation

In this section, we assemble all the components detailed above to form the final prototype of the fully integrated 60 GHz front-end receiver. The latter is shown in photograph at **Figure 18**. It therefore includes an 8 × 2 antenna array, a low-noise amplifier (LNA), a six-port circuit, and power detectors, integrated on a same 2.54 cm × 2.54 cm ceramic substrate. In summary, its function and principle of operation are as follows: the RF signal enters at port 6, after being received by a 16-element patch antenna array (16.8 dB Gain) and amplified by the TGA4600 LNA from TriQuint Semiconductor (57–65 GHz, 13 dB Gain, and 4 dB noise figure). The reference signal from the local oscillator (LO) enters at port 5 through a microstrip to WR12 rectangular waveguide (RW) transition. In order to recover the low IF or the baseband signals, the four six-port outputs are connected to the RF power detectors.

The fabricated 60 GHz six-port front-end receiver has been tested using the test bench illustrated in the block diagram of **Figure 19** and the corresponding photograph at **Figure 20**. In the transmitting part, the HP 8360 Series Synthesized Sweeper output is connected to a commercial K-Band power amplifier with a gain of around 10 dB. Limited by the upper output frequency range of the frequency synthesizer (40 GHz), an additional millimeter-wave frequency multiplier module (x3), model SFP-123KF-S1, from SAGE Millimeter, Inc., is then used to achieve a frequency around 61.71 GHz (20.57 GHz × 3). The obtained signal is combined

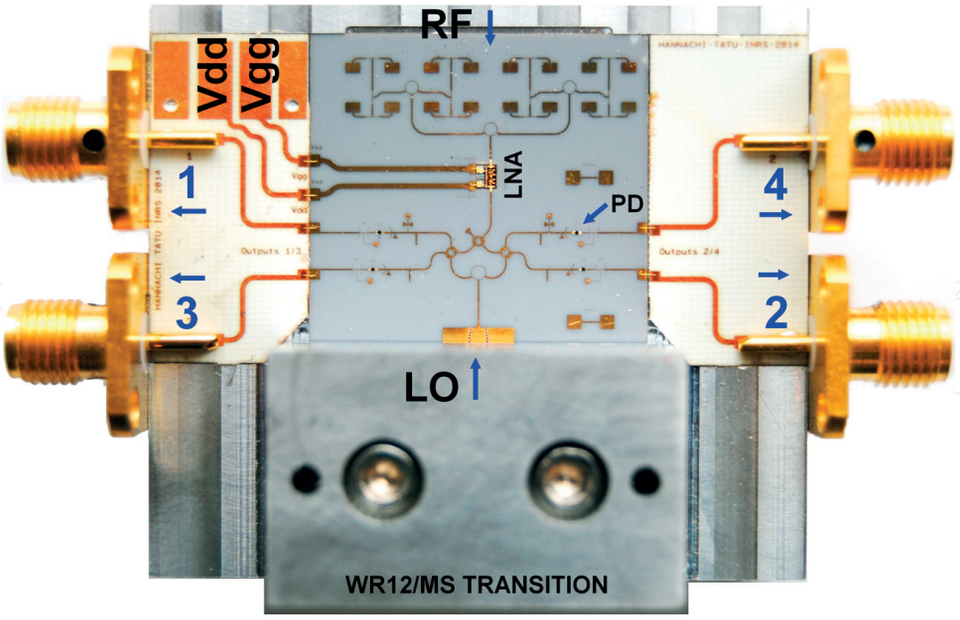

Figure 18. The fabricated six-port front-end receiver prototype.

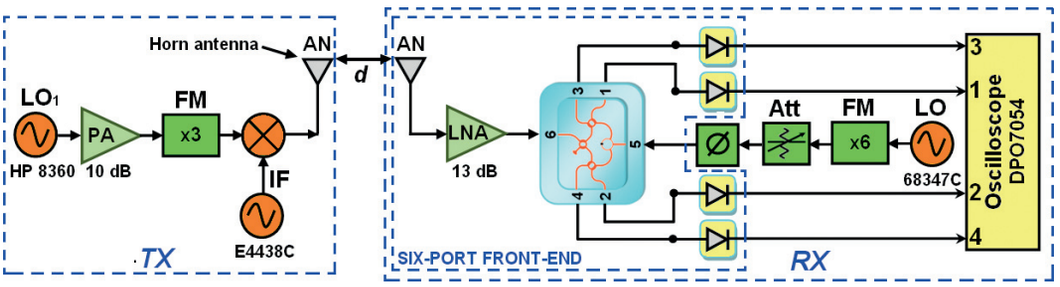

Figure 19. Block diagram of the test bench for the fabricated six-port front-end receiver prototype.

with the 600 MHz intermediate frequency (IF) signal from Agilent E4438 source, through a balanced RF mixer. In order to transmit the modulated signal, a horn antenna operating at the 60 GHz band, with a gain of about 22 dBi, is also employed.

In the receiving part, a frequency multiplier (x6) is used to generate the LO signal having the frequency of 62.19 GHz, at port 5 of the fabricated 60 GHz front-end receiver prototype (signal coming from Anritsu 68347C Synthesized Signal Generator at 10.38 GHz (6 × 10.38 GHz)). An attenuator and phase shifter are also used to control the power level and phase of the LO signal in millimeter-wave band (V-band), respectively. The four output signals, from the 60 GHz front-end receiver prototype, are displayed and recorded using a Tektronix digital phosphor oscilloscope (DPO7054), with 1 MΩ input impedance.

The demodulation results of various signals, from 4 to 32 symbols, are therefore obtained as shown in **Figure 21**. As can be observed in these captures, the symbols of BPSK, 8PSK, and 16PSK demodulations are distributed evenly around the circle. Likewise, for the QPSK constellation diagram, a quasi-perfectly square shape is achieved, whereas for the 16QAM and

http://dx.doi.org/10.5772/intechopen.72715

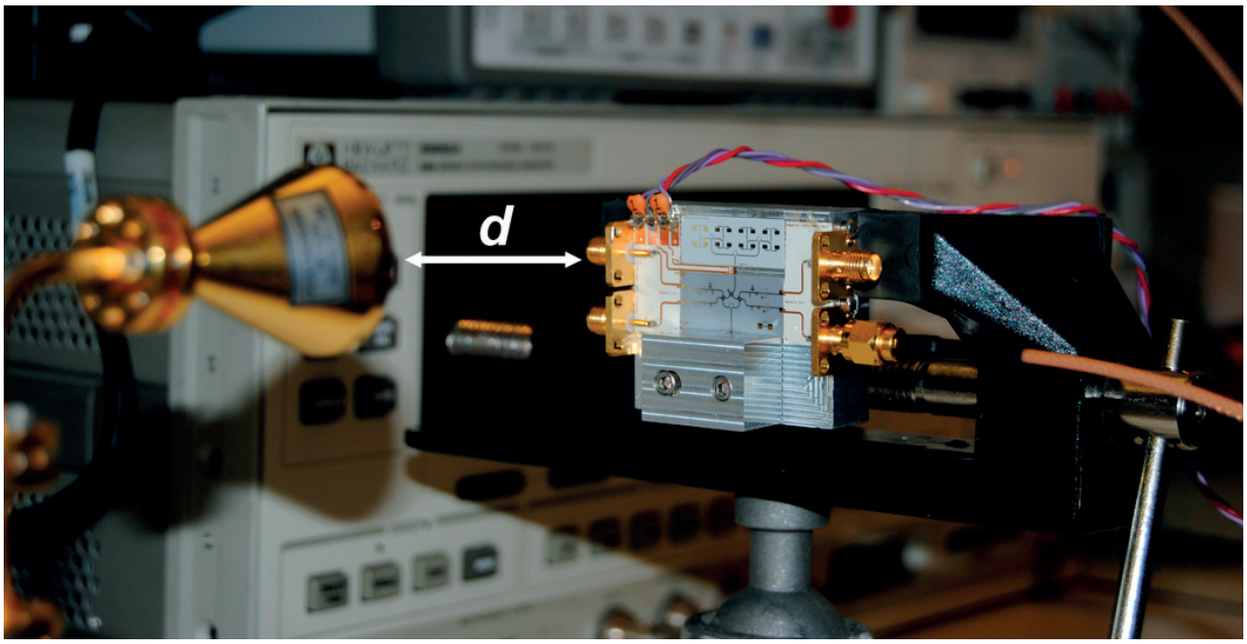

Figure 20. Photograph of the test bench for the fabricated 60 GHz six-port front-end receiver.

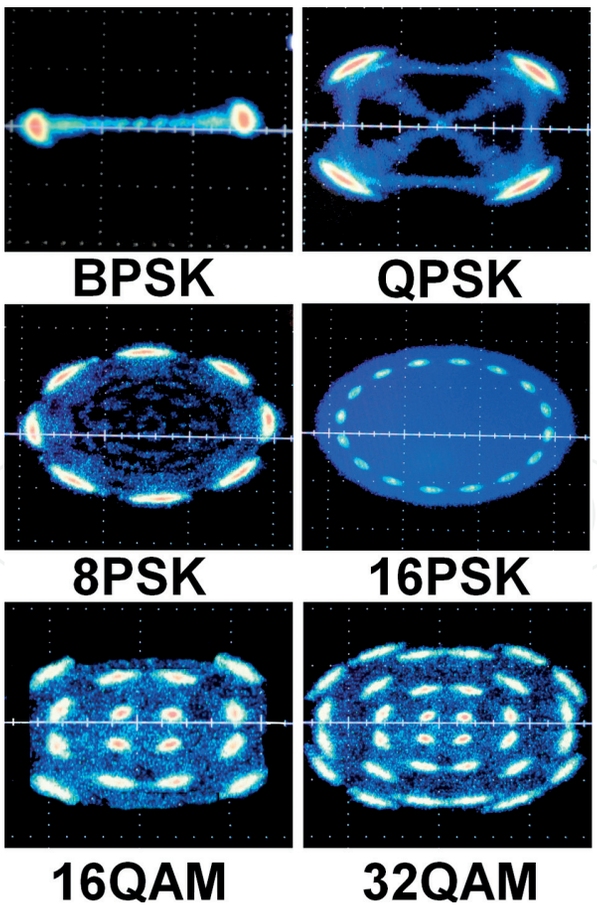

Figure 21. Experimental constellation results of the demodulated MPSK/MQAM signals.

32QAM, the points are almost equidistant, proving the front-end discrimination's qualities in both amplitude and phase, according to the six-port demodulation theory [12]. As can be seen, the phase and amplitude errors are minimal, not exceeding a few percent for each constellation point. It should be pointed out that those errors are mainly due to synchronization of transmitting and receiving equipment (phase noise), as well as the fabrication tolerances (symmetry of the constellation points).

4. Conclusion

The research on the front-end receiver designs in the unlicensed 60 GHz frequency band has been going on for several years now. Although a multitude of 60 GHz front-end configurations have been published in literature, they are not consequently optimized for low power consumption. In this context, the multi-port technique has been proposed as an attractive solution enabling the design of low-cost and compact wireless communication receivers at microwave and millimeter-wave frequency bands.

This chapter describes in detail the design of a low-power 60 GHz direct conversion front-end receiver based on the multi-port (six-port) concept, using a less costly MHMIC fabrication process. The demodulation performances of the proposed front-end receiver structure have been experimentally proven through various M-PSK/M-QAM demodulated signals. The obtained demodulation results, demonstrating the ability of the proposed 60 GHz six-port front-end receiver to directly demodulate PSK or QAM millimeter-wave signals to baseband, or even to down-convert them in quadrature to a given intermediate frequency (IF), create a real expansion opportunity to the future compact, low-power, and low-cost 60 GHz wireless communication systems.

Acknowledgements

The authors would like to acknowledge the financial support of the National Sciences and Engineering Research Council (NSERC) and the fabrication support of the "Centre de Recherche en Électronique Radiofréquence" (CREER), Montréal, funded by the "Fonds du recherche du Quebec—Natures and Technologies" (FRQNT).

Author details

Chaouki Hannachi* and Serioja Ovidiu Tatu

*Address all correspondence to: hannachi@emt.inrs.ca

Energy Materials Telecommunications Research Center, National Institute of Scientific Research, INRS, Montreal, Canada

References

[1] Ghannouchi FM, Mohammadi A. The Six-Port Technique with Microwave and Wireless Applications. Norwood: Artech House; 2014. 250p. ISBN: 9783540495215

[2] Hannachi C, Tatu SO. An improved-performance V-band six-port receiver for future 5G short-range wireless communications. In: Proceedings of the IEEE Topical Conference on Wireless Sensors and Sensor Networks (WiSNet); 15-18 January 2017; Phoenix. Arizona. pp. 2473-4624

[3] Hannachi C, Tatu SO. A new compact V-band six-port down-converter receiver for high data rate wireless applications. In: Proceedings of the IEEE Topical Conference on Wireless Sensors and Sensor Networks (WiSNet); 25-28 January 2015; San Diego, CA, USA. pp. 26-28

[4] Tatu SO, Moldovan E, Brehm G, Wu K, Bosisio RG. Ka band direct digital receiver. IEEE Transactions on Microwave Theory and Techniques. 2002;**50**:2436-2442. DOI: 10.1109/TMTT.2002.804646

[5] Tatu SO, Moldovan E, Wu K, Bosisio RG, Denidni T. Ka-band analog front-end for software-defined direct conversion receiver. IEEE Transactions on Microwave Theory and Techniques. 2005;**53**:2678-2776. DOI: 10.1109/TMTT.2005.854181

[6] Moldovan E, Tatu SO. Design and characterization of novel W-band wide-band couplers and six-port circuit. In: Proceedings of the European Microwave Week (EuMW); 6-11 September 2015; Paris. France. pp. 279-282

[7] Engen GF. The six-port reflectometer: An alternative network analyzer. IEEE Transactions on Microwave Theory and Techniques. 1977;**25**:1075-1080. DOI: 10.1109/MWSYM.1977.1124352

[8] Engen GF, Hoer CA. Application of an arbitrary 6-port junction to power-measurement problems. IEEE Transactions on Instrumentation and Measurement. 1972;**21**:470-474. DOI: 10.1109/TIM.1972.4314069

[9] Hannachi C, Hammou D, Djerafi T, Ouardirhi Z, Tatu SO. Complete characterization of novel MHMICs for V-band communication systems. Journal of Electrical and Computer Engineering. 2013;**2013**:1-9. DOI: 10.1155/2013/686708

[10] Swapnil D, Ankit G, Harsh N. A review of laser micromachining. International Journal of Engineering Science and Computing. 2016;**6**:2416-2420. DOI: 10.4010/2016.574

[11] Tatu SO, Moldovan E, Affes S. Multi-port front-end and transceivers for V-band multi-gigabit/s communication systems. In: Digital Front-End in Wireless Communications and Broadcasting Circuits and Signal Processing. Cambridge University Press; 2011. pp. 707-732. DOI: 10.1017/CBO9780511744839.025

[12] Hannachi C, Moldovan E, Ouardirhi Z, Tatu SO. V-band six-port quadrature demodulator: Error vector magnitude analysis. In: Proceedings of 8th Global Symposium on Millimeter-Waves (GSMM 2015); 25-27 May 2015; Montreal, Canada. pp. 1-3

[13] Östh J. Study of Six-port Modulators and Demodulators for High-speed Data Communications [thesis]. Linköping: Linköping University; 2012

[14] Hammou D, Moldovan E, Tatu SO. Novel MHMIC millimeter-wave power divider/combiner. In: Proceedings of 2011 IEEE Canadian Conference on Electrical and Computer Engineering (CCECE 2011); 8-11 May 2011; Niagara Falls, Ontario. pp. 280-283

[15] Hannachi C, Zouggari B, Cojocaru RI, Djerafi T, Tatu SO. A V-band high dynamic range planar integrated power detector: Design and characterization process. Microwave and Optical Technology Letters. 2017;**59**:2742-2748. DOI: 10.1002/mop.30809

[16] Hrobak M. Critical mm-Wave Components for Synthetic Automatic Test Systems. Berlin: Springer; 2015. 425p. DOI: 10.1007/978-3-658-09763-9

[17] Lee KF, Chen W. Advances in Microstrip and Printed Antennas. Hoboken: Wiley; 1997. 624p. ISBN: 978-0-471-04421-5

[18] Hannachi C, Zouggari B, Tatu SO. A compact, high gain and high efficiency 8×2 patch antenna array for 60 GHz communication systems. In: Proceedings of 17th International Symposium on Antenna Technology and Applied Electromagnetics (ANTEM 2016); 10-14 July 2015; Montreal, Canada. pp. 1-2